CONDENSED MATTER PHYSICS

Voltage-induced ferromagnetism in a diamagnet

Jeff Walter[1,2], Bryan Voigt[1], Ezra Day-Roberts[3], Kei Heltemes[1,2], Rafael M. Fernandes[3], Turan Birol[1], Chris Leighton[1]*

Increasingly impressive demonstrations of voltage-controlled magnetism have been achieved recently, highlighting potential for low-power data processing and storage. Magnetoionic approaches appear particularly promising, electrolytes and ionic conductors being capable of on/off control of ferromagnetism and tuning of magnetic anisotropy. A clear limitation, however, is that these devices either electrically tune a known ferromagnet or electrically induce ferromagnetism from another magnetic state, e.g., antiferromagnetic. Here, we demonstrate that ferromagnetism can be voltage-induced even from a diamagnetic (zero-spin) state suggesting that useful magnetic phases could be electrically induced in "nonmagnetic" materials. We use ionic liquid–gated diamagnetic FeS_2 as a model system, showing that as little as 1 V induces a reversible insulator-metal transition by electrostatic surface inversion. Anomalous Hall measurements then reveal electrically tunable surface ferromagnetism at up to 25 K. Density functional theory–based modeling explains this in terms of Stoner ferromagnetism induced via filling of a narrow e_g band.

INTRODUCTION

Magnetic materials have been linchpins of high technology for decades. Contemporary examples include hard disk drives and magnetic random access memories, although ongoing advances in spintronics have created myriad additional possibilities, in sensing, data storage, and processing (*1*). One such advance is the capability to control ferromagnetic magnetization with electrical currents, in addition to magnetic fields, via spin-transfer (*2*) and spin-orbit torques (*3*, *4*). Field- and current-based manipulation of ferromagnetism intrinsically involves power consumption, however, which is a critical limiting factor in data storage and processing (*1*, *5*). This situation has focused great attention on voltage-based (i.e., electric field–based) control of magnetism, with potential for much lower power consumption (*1*, *5*–*7*).

While multiple approaches to voltage-controlled magnetism exist, magnetoionics, where electric field–induced ion motion is used to manipulate magnetism, appears particularly promising (*6*–*8*). The electric double-layer transistor (EDLT; Fig. 1A) is foundational to this effort, as it has proven highly effective in voltage control of insulator-metal and superconducting transitions and is now being used in magnetoionics (*6*–*9*). An EDLT is formed by replacing the dielectric in a field-effect transistor with an electrolyte, often an ionic liquid (IL). When a gate voltage (V_g) is applied between the magnetic material and a metallic gate, IL cations or anions (depending on the V_g polarity) drift to the surface of the magnet, where they accumulate (Fig. 1A, right). The electric field created is then screened by induction of a two-dimensional (2D) sheet of electrons/holes in the magnetic material, forming an electric double layer (EDL). This EDL is essentially a nanoscale capacitor, resulting in tens of microfarad per square centimeter capacitances and electron/hole densities up to 10^{15} cm^{-2} at just a few volts (*8*–*10*). This is sufficient to induce and control electronic phase transitions and order, including magnetism (*8*–*10*).

EDLT-based voltage control of ferromagnetism is advancing rapidly. Control of the Curie temperature (T_C) of ferromagnets, for example, has progressed from V_g-induced shifts of ~30 K in IL-gated perovskite manganites (*11*) to 110 K in ultrathin Co (*12*) to >150 to 200 K in perovskite cobaltites (*13*–*16*). The reversible voltage induction of ferromagnetism from nonferromagnetic states, such as antiferromagnetic $LaMnO_3$ (*17*) or $SrCoO_{2.5}$ (*14*), has also been demonstrated. The gating mechanisms in these EDLTs are often not simply electrostatic, as in Fig. 1A, but involve electrochemistry (*8*). Oxide ionic gating effects based on creation and annihilation of oxygen vacancies (*13*–*15*, *18*–*20*) and insertion and extraction of hydrogen (*14*, *21*, *22*) are now known, for example. This has spawned expansion from IL-based EDLTs to devices based on ion gels, solid electrolytes, ionic conductors, etc. (*6*–*8*, *10*), applied beyond insulators and semiconductors to thin film ferromagnetic metals, for example (*12*, *23*–*29*). Notable achievements include sizable voltage-based modulation of T_C, magnetization, coercivity, and magnetic anisotropy (*6*–*8*, *11*–*17*, *23*–*29*), in addition to encouraging progress with reversibility and speed (*27*, *30*).

While impressive, these advances are subject to a clear limitation. Specifically, they involve either voltage control of a known ferromagnet (*11*, *12*, *23*–*29*) or voltage-induced ferromagnetism from some other magnetic state (*13*, *14*, *16*, *17*, *31*), be it ordered (e.g., antiferromagnetic) or disordered (paramagnetic). This raises a simple question with deep implications: Can ferromagnetism be voltage-induced from a "nonmagnetic" state, i.e., a diamagnet, with a zero-spin electronic configuration? We address this here using IL-gated single crystals of diamagnetic FeS_2, i.e., Fool's Gold. This is a pyrite structure 0.95-eV gap semiconductor with $t_{2g}^6 e_g^0$ electronic configuration and well-established zero-spin diamagnetism (*32*–*34*). What makes FeS_2 ideal for such studies is that alloying with ferromagnetic CoS_2 (electronic configuration, $t_{2g}^6 e_g^1$) to produce $Fe_{1-x}Co_xS_2$ induces ferromagnetism at as little as 1% Co (*35*, *36*), eventually reaching a state with $T_C \approx 150$ K in $Fe_{0.2}Co_{0.8}S_2$ (*37*–*39*). Interfacial charge transfer in pyrite-containing heterostructures has also been predicted to induce ferromagnetism in FeS_2 (*40*). While likely not unique, diamagnetic FeS_2 thus exists in unusual proximity to a ferromagnetic instability, rendering it ideal for investigation of the plausibility of voltage-induced ferromagnetism in a diamagnetic system.

[1]Department of Chemical Engineering and Materials Science, University of Minnesota, Minneapolis, MN 55455, USA. [2]Department of Physics, Augsburg University, Minneapolis, MN 55454, USA. [3]School of Physics and Astronomy, University of Minnesota, Minneapolis, MN 55455, USA.
*Corresponding author. Email: leighton@umn.edu

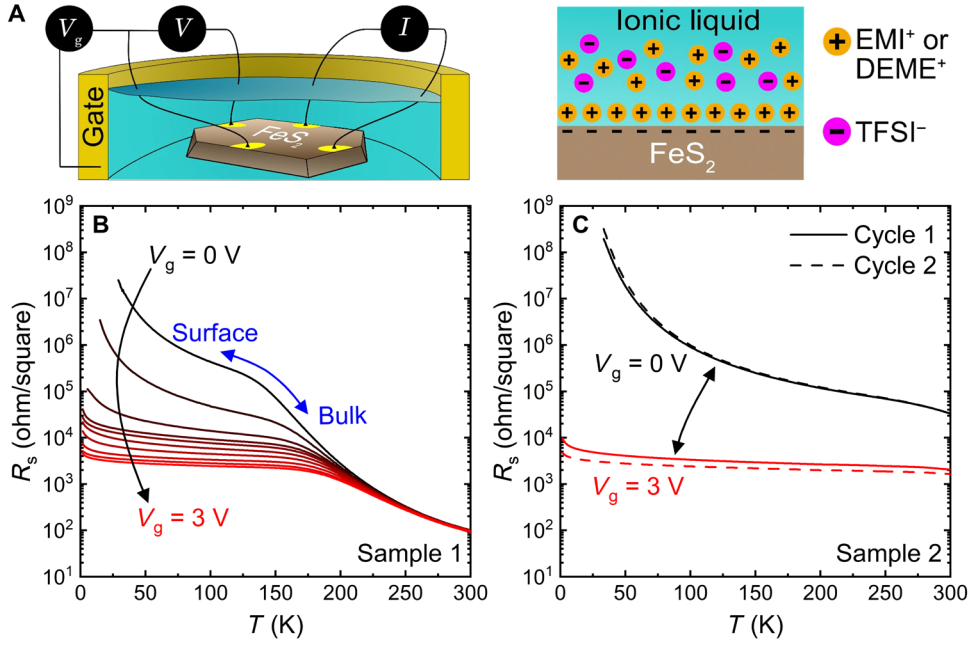

Fig. 1. Measurement schematic and reversible voltage-induced surface insulator-metal transition. (**A**) Schematic of the ionic liquid (IL) gating device (left) and FeS_2 surface electric double layer (EDL) (right). V_g, V, and I are the gate voltage, measurement voltage, and excitation current, respectively. The FeS_2 single crystal, gold contacts, metallized gate electrode/liquid container, the IL, the IL cations and anions, and the induced electrons at the FeS_2 surface are shown. (**B**) Temperature (T) dependence of the FeS_2 sheet resistance (R_s) at multiple V_g between 0 and +3.0 V (0, +1.0, +1.1, +1.2, +1.3, +1.4, +1.6, +1.8, +2.0, and +3.0 V) for sample 1. The bulk to surface conduction crossover at $V_g = 0$ is labeled. (**C**) $R_s(T)$ for sample 2 at $V_g = 0$ and +3.0 V through the two consecutive V_g cycles indicated in the legend. EMI/TFSI [1-ethyl-3-methylimidazolium bis(trifluoro-methylsulfonyl) imide] was used for all data in this figure.

RESULTS AND DISCUSSION

As described in Materials and Methods, EDLTs based on pyrite FeS_2 single crystals (see fig. S1 and table S1 for structural and chemical characterization details) were fabricated using a metallized cylinder as both the gate electrode and IL container (Fig. 1A). Figure 1B shows the resulting temperature (T) dependence of the sheet resistance (R_s) of a representative EDLT (sample 1) at V_g values between 0 and +3 V (i.e., in electron accumulation mode). At $V_g = 0$, typical single-crystal FeS_2 behavior is observed, semiconducting transport ($dR_s/dT < 0$) occurring down to ~150 K, where $R_s(T)$ flattens before increasing at low T. This arises due to the surface conduction that is now established in FeS_2 crystals, where the semiconducting interior, which is lightly n-doped (e.g., 10^{16} cm^{-3} at 300 K) by S vacancies, is shunted at low T by a heavily doped (e.g., 10^{20} cm^{-3} to 10^{21} cm^{-3}) p-type surface layer (see fig. S2 for further details) (*41*–*44*). The surface Fermi level pinning and band bending required for this likely arise from surface states, with important implications for pyrite photovoltaics (*41*, *42*, *44*). More important in the current context, application of V_g up to +3 V is seen in Fig. 1B to result in marked decreases of the low T resistance (by ~10^4-fold at 30 K, extrapolating to much more at lower T). R_s falls beneath $h/e^2 \approx 26$ kilohm, $R_s(T)$ becoming flat by +3 V, aside from a weak low T upturn. As discussed below, detailed $R_s(T, H)$ data and analyses (where H is the applied magnetic field) establish that this occurs due to a transition from Efros-Shklovskii variable-range hopping (*45*) to weak localization (*46*) at ≥1.2 V. Note that the 300 K (bulk) resistance in Fig. 1B is barely affected by V_g, meaning that this strongly localized to essentially metallic transition occurs on the FeS_2 surface. This occurs at positive V_g, implying inversion of the initially p-type surface (*44*) to an n-type metal, as confirmed below.

The reversibility of the observed V_g-induced surface insulator-metal transition is explored in Fig. 1C using a second sample (sample 2). This sample has lower bulk n-doping (see Materials and Methods), resulting in higher R_s (300 K) and thus a higher bulk-to-surface crossover temperature (>300 K). The solid black and red lines in Fig. 1C depict the 0- and +3 V behavior during the initial V_g cycle, where the 30 K resistance drops by a factor of ~10^5. Returning V_g to zero (dashed black line, cycle 2) then results in $R_s(T)$ essentially identical to the initial state, reapplication of +3 V (dashed red line, cycle 2) inducing very similar $R_s(T)$ to initial gating. This extraordinary level of reversibility, in a system where even minor surface structural or chemical modifications result in large changes in surface conduction (*41*, *42*), provides strong evidence of a reversible, predominantly electrostatic gating mechanism (Fig. 1A), as opposed to the electrochemical mechanisms frequently encountered (*8*).

The data of Fig. 1B replotted to permit Zabrodskii analysis are shown in Fig. 2A. In this approach, $\ln W$ is plotted versus $\ln T$, where W, the reduced activation energy, is defined as $W = -d\ln R_s/d\ln T$. This linearizes $R_s = R_0\exp(T_0/T)^m$, where T_0 is a characteristic temperature, R_0 is $R_s(T \rightarrow \infty)$, and the exponent m provides insight into conduction mechanisms. The rapid decrease in $\ln W$ on initial cooling in Fig. 2A reflects the bulk to surface conduction crossover, which is followed by a clear progression with V_g in the low T limit. At $V_g = 0$ and +1 V, positive $\ln W$ values that increase linearly with decreasing $\ln T$ are seen in Fig. 2A, with a slope $m \approx 0.5$ (blue solid line). As in prior work on ungated FeS_2 crystals (*42*, *47*), this indicates Efros-Shklovskii variable-range hopping (*45*), i.e., $R_s = R_0\exp(T_0/T)^{1/2}$, on the insulating side of the insulator-metal transition. As V_g is increased above 1.1 V, however, $\ln W$ becomes negative and T independent,

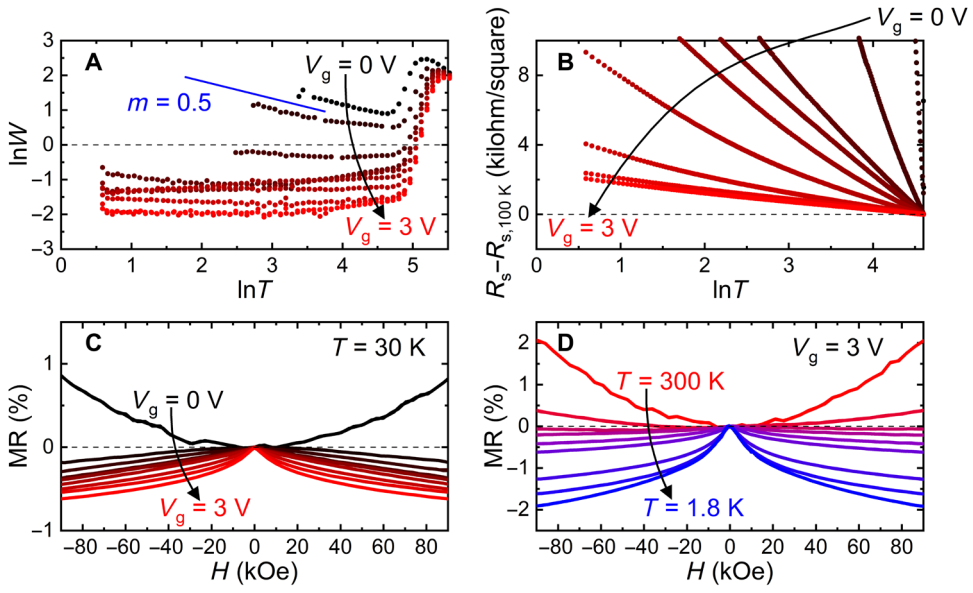

Fig. 2. Details of the voltage-induced insulator-metal transition. (**A**) Zabrodskii analysis of the temperature (T) dependence of the sheet resistance (R_s) for the sample 1 data shown in Fig. 1B. ln$W$ is plotted versus ln$T$, where $W = -d\ln R_s/d\ln T$, at gate voltages (V_g) between 0 and +3.0 V (0, +1.0, +1.1, +1.2, +1.3, +1.4, +1.6, +1.8, +2.0, and +3.0 V). The solid blue line corresponds to $m = 0.5$, i.e., Efros-Shklovskii variable-range hopping. (**B**) ($R_s - R_{s,100\,K}$) versus ln$T$, where $R_{s,100K}$ is $R_s(T = 100$ K), for the same $R_s(T, V_g)$ curves in (A). (**C**) Magnetoresistance (MR) versus perpendicular magnetic field (H) at 30 K for the same V_g shown in (A) and (B). (**D**) MR(H) at $V_g = 3.0$ V for T between 300 and 1.8 K (300, 240, 180, 120, 60, 30, 10, 5, and 1.8 K). All data are for sample 1 using EMI/TFSI.

indicating a crossover to nonactivated transport, i.e., effectively metallic behavior. Figure 2B further emphasizes this by plotting ($R_s - R_{s,100K}$) versus ln$T$ (where $R_{s,100K}$ is the value of R_s at 100 K) at each V_g. The rapid increase in R_s on cooling at low V_g is seen to give way to a weak, approximately ln$T$ dependence at high V_g. This behavior is expected for weakly localized transport in a 2D surface layer (*46*), which we show below to be the case in these EDLTs.

Further support for these conclusions is provided by magnetoresistance (MR) measurements (with H perpendicular to the crystal surface), as in Fig. 2C at 30 K. At $V_g = 0$, parabolic positive MR occurs, consistent with the Efros-Shklovskii variable-range hopping (*45*) deduced from Fig. 2A. As V_g is increased, the MR switches to negative, taking on a form characteristic of weak localization, again consistent with Fig. 2 (A and B). Figure 2D then illustrates MR(T) at fixed $V_g = 3$ V, which is also qualitatively consistent with our analysis of $R_s(T)$. Specifically, positive parabolic MR at high T (due to the ordinary MR effect when bulk semiconducting conduction dominates) crosses over to negative MR at low T (when weakly localized surface conduction dominates). Figure 2 thus evidences a positive-V_g–induced transition in the low T surface-dominated conduction from strongly localized variable-range hopping to effectively metallic/weakly localized transport at $V_g \geq 1.2$ V.

The magnetic behavior in the V_g-induced effectively metallic FeS_2 surface state is explored in Fig. 3 via anomalous Hall effect measurements. The 30 K V_g dependence of the transverse (i.e., Hall) conductance versus perpendicular magnetic field (H) is shown in Fig. 3A. This is defined as $G_{xy} = R_{xy}/R_{s,0}{}^2$, where R_{xy} is the transverse resistance and $R_{s,0}$ is the zero field sheet resistance. The data in Fig. 3A were acquired on sample 1 at the same V_g values as in Figs. 1B and 2, the inset showing a low H view. G_{xy} is negligible at $V_g = 0$, as the Hall effect in this sample is suppressed at low T by hopping conduction (fig. S2) (*42*, *47*). Increasing V_g to +1.6 V induces a clear Hall effect, however, with both negative slope and distinct curvature (Fig. 3A, inset). The negative slope is important, as it suggests that at this V_g (which is effectively metallic from Figs. 1B and 2), inversion of the p-type surface to n-type has occurred. Further increasing V_g to +1.8, +2, and +3 V (Fig. 3A, main panel) then leads to the emergence of a very different state with a much larger, positive slope, nonlinear Hall effect. $G_{xy}(H)$ is sigmoidal, immediately suggestive of the anomalous Hall effect, the positive slope being consistent with the anomalous Hall coefficient in ferromagnetic $Fe_{1-x}Co_xS_2$ (*36*).

To probe for possible hysteresis, Fig. 3B shows V_g-dependent (from +1.1 to +3 V) $G_{xy}(H)$ in the same sample at 1.8 K, with the low-field behavior highlighted in the inset. Clear coercivity ($H_c = 700$ Oe) and remanence occur at the highest V_g (see inset). The data of Figs. 1 to 3 thus establish gate induction of an effectively metallic FeS_2 surface state with a strong, sigmoidal $G_{xy}(H)$, a sign consistent with the anomalous Hall coefficient of $Fe_{1-x}Co_xS_2$ and both coercivity and remanence. We take these observations as strong evidence for electric field–induced ferromagnetism in this diamagnet. The data of Fig. 3C establish repeatability, demonstrating finite low temperature H_c at high V_g in anomalous Hall data on three samples (samples 1, 2, and 3). Note that the cutoff H_c value in Fig. 3C (which has a $\log_{10}$ scale) is 7 Oe, the minimum value detectable in our superconducting magnet-based measurements. We thus take the point where H_c falls to ≤ 7 Oe as a good estimate of T_C. At a high V_g of +3 V, the H_c (1.8 K) and T_C values vary somewhat from sample to sample (from 400 to 2300 Oe and 10 to 24 K), although both increase monotonically with V_g in a single sample: Fig. 3C shows sample 3 at +2, +3, and +4 V, for example, where T_C is 10, 12, and 15 K, respectively. The crystal-to-crystal variations in the gate-induced surface ferromagnetic parameters may be related to variations in surface conduction in FeS_2 single crystals, which are highly sensitive to the surface structure and chemistry (*42*); this is a topic worthy of further

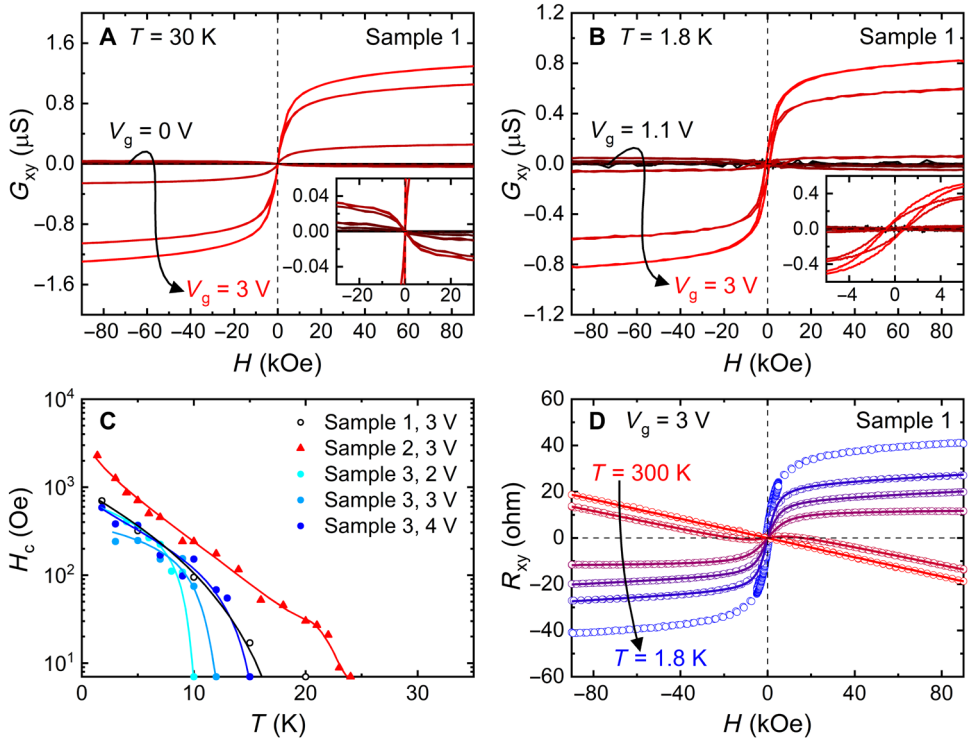

Fig. 3. Voltage-induced ferromagnetism at the FeS_2 surface. Transverse (Hall) conductance (G_{xy}) versus applied magnetic field (H) for sample 1 at multiple gate voltages (V_g); data are shown at (**A**) 30 K (0, +1.0, +1.1, +1.2, +1.3, +1.4, +1.6, +1.8, +2.0, and +3.0 V) and (**B**) 1.8 K (+1.1, +1.2, +1.3, +1.4, +1.6, +1.8, +2.0, and +3.0 V). Note the low H insets. (**C**) Temperature (T) dependence of the coercivity (H_c, $\log_{10}$ scale) in the ferromagnetic state of samples 1, 2, and 3 at multiple V_g. (**D**) H dependence of the transverse (Hall) resistance (R_{xy}) of sample 1 at V_g = 3.0 V (open circle symbols), at multiple T, along with fits to the Langevin-based model described in the text (lines). Data are shown at 300, 280, 200, 100, 20, and 1.8 K. EMI/TFSI was used in all data in this figure.

study. The highest T_C achieved was 24 K in sample 2 at 3 V, where H_c (1.8 K) reached 2300 Oe.

To further explore the temperature evolution of the high V_g ferromagnetism, Fig. 3D plots $R_{xy}(H)$ in sample 1 from 1.8 (blue open circles) to 300 K (red open circles). The large positive slope anomalous Hall effect at low T is seen to eventually give way to a linear negative slope ordinary Hall effect at 300 K. However, two effects are convoluted here: the loss of surface magnetism and the crossover to conduction dominated by the n-type interior. What is remarkable in Fig. 3D is that, while T_C = 16 K, the anomalous Hall effect remains dominant to 200 K and is detectable (on the ordinary Hall background) at 280 K. While H_c vanishes at 16 K, clear contributions to anomalous Hall thus exist at up to 280 K (i.e., 20 times T_C), suggesting that ferromagnetic correlations persist to unusually high T. This is highlighted in Fig. 4 (A and B), which shows the T dependence of $|dR_{xy}/dH|_{H\to 0}$ and R_{xy}^F. The first of these quantities is simply the low-field Hall slope, while the second is the R_{xy} obtained by linearly extrapolating high H data (>70 kOe) to H = 0; both thus probe the nonlinear magnetic contribution to $R_{xy}(H)$. Both quantities fall rapidly at T_C (see the dashed vertical line in Fig. 4, A and B) but exhibit long, near-linear high T tails, reaching zero only at 300 K, where bulk conduction dominates. This T dependence is in stark contrast to standard Curie-Weiss behavior in an interacting paramagnet, as illustrated by the solid line in Fig. 4A of the form $C/(T - 16\ \mathrm{K})$ (where C is a constant).

One possible interpretation of Fig. 4 (A and B) is that the induced FeS_2 surface ferromagnetism occurs close to the 2D limit, thus suppressing T_C despite strong ferromagnetic correlations. While the cubic magnetocrystalline anisotropy of $Fe_{1-x}Co_xS_2$ is unknown at low x, at x = 1 (i.e., CoS_2), it is parameterized by low T anisotropy constants K_1 and K_2 of only -2.5×10^4 erg cm^{-3} and ~0 erg cm^{-3}. (*48*) This is an order of magnitude lower than even face-centered cubic Ni. (*49*) The ferromagnetism electrically induced in FeS_2 could thus be expected to be weakly anisotropic, i.e., of Heisenberg type (*50*). Mermin-Wagner physics (*51*) would then apply, limiting the 2D T_C despite strong ferromagnetic interactions. In this context, we note that electrostatic calculations (fig. S3) indicate that 90% of the induced electrons in these EDLTs are confined within (at most) ~2 nm (i.e., four unit cells) of the surface. In terms of direct extraction of information on magnetic anisotropy from our data, some weak perpendicular magnetic anisotropy apparently occurs based on the finite H_C and remanence in Fig. 3B. Simple estimates using $H_C \approx 1$ kOe (Fig. 3C) and saturation magnetization ~0.2 μ_B per Fe (see below, Fig. 5) yield low effective uniaxial anisotropy values, ~10^4 erg cm^{-3}. Further work will be needed to fully characterize magnetic anisotropy in the voltage-induced ferromagnetic state, including understanding the origin of the perpendicular magnetic anisotropy. We note, in this context, that the high-field curvature in Fig. 3B may indicate an additional paramagnetic contribution, rather than ferromagnetic anisotropy.

An alternative interpretation of the temperature dependence in Fig. 3D involves superparamagnetism. The zero-coercivity sigmoidal-shaped curves seen above 16 K in Fig. 3D can be well fit to $R_{xy} = k_1 L(\mu_c\mu_0 H/k_B T) + k_2\mu_0 H$, where L is the Langevin function, μ_c is a

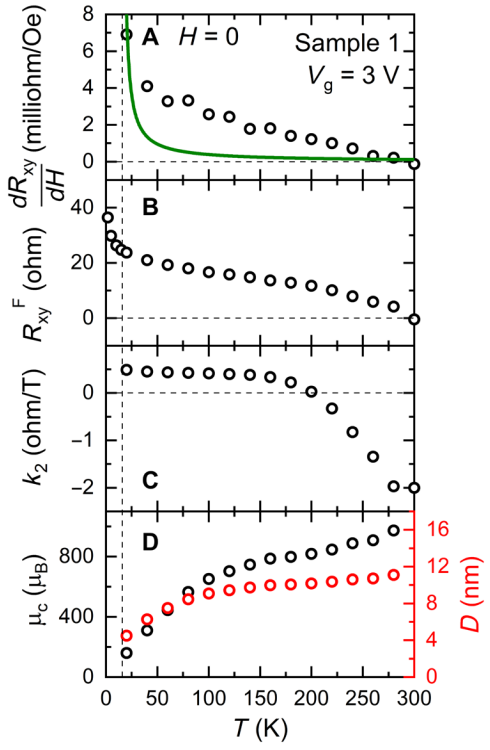

Fig. 4. Analysis of temperature dependence of the anomalous Hall effect. Temperature (T) dependence of (**A**) $[dR_{xy}/dH]_{H=0}$ (the field derivative of the transverse resistance as $H \to 0$) and (**B**) R_{xy}^{F} [i.e., the transverse resistance obtained by extrapolating the high H $R_{xy}(H)$ curve to $H = 0$] in sample 1 at $V_g = 3.0$ V. The solid green curve in (A) illustrates Curie-Weiss behavior. (**C** and **D**) T dependence of the parameters extracted from the Langevin-based fitting described in the text, including the parameter k_2 (C) and the cluster magnetic moment (μ_c) and deduced diameter (D) (D, left and right axis, respectively). As described in the text, k_2 reflects a paramagnetic background and the negative bulk ordinary Hall effect at low and high T, respectively. D is deduced from μ_c assuming 0.2 μ_B per Fe and an accumulation layer with a thickness of 2 nm, resulting in disk-shaped clusters. The vertical dashed line indicates the Curie temperature (16 K). EMI/TFSI was used in all data in this figure.

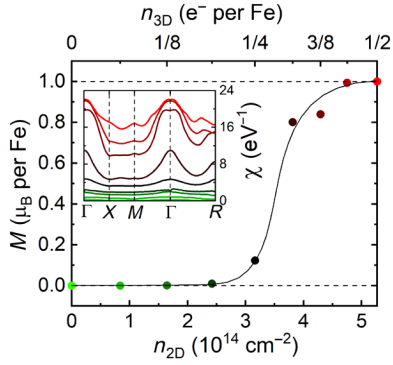

Fig. 5. Theoretical results on voltage-induced ferromagnetism at the FeS_2 surface. Calculated induced ferromagnetic magnetization (M) versus added 2D projected electron density, n_{2D}. The top axis shows the conversion to electrons per Fe ion (n_{3D}); this axis is not linear due to cell volume changes that take place with electron addition (the structure is relaxed at each density). The data points are color-coded to the solid curves in the inset, which show the wave vector ($\underline{k}$) dependence of the susceptibility (χ) at each calculated electron density. Γ, X, M, and R correspond to $\underline{k} = [0, 0, 0]$, [1, 0, 0], [1, 1, 0], and [1, 1, 1] in momentum space, respectively. A peak emerges at the Γ point, corresponding to long-range–ordered ferromagnetism ($\underline{k} = 0$). Note that n_{2D} values in the main panel assume an accumulation thickness of one unit cell. Surface n_{2D} values above 3×10^{14} cm^{-2} result in estimated accumulation layer thicknesses at the unit cell level (see fig. S3), rendering experiment and Fig. 5 comparable.

cluster magnetic moment, μ_0 is the vacuum permeability, and k_B is Boltzmann's constant. This describes the H and T dependence of the magnetization with a Langevin function (as expected in a simple superparamagnet above its blocking temperature), k_1 being related to the anomalous Hall coefficient and k_2 capturing a paramagnetic background and the ordinary Hall effect. As shown by the solid lines in Fig. 3D, good fits can be obtained, indicating that $R_{xy}(H)$ at any $T > 16$ K can be described as a Langevin superparamagnet. Figure 4C further illustrates that the extracted $k_2(T)$ behaves rationally, crossing from positive at low T (likely a paramagnetic background) to negative at high T (due to the bulk negative ordinary Hall coefficient). The extracted μ_c values (Fig. 4D) of ~200 to 1000 μ_B are also plausible. Using again an approximate magnetization of 0.2 μ_B per Fe (see below, Fig. 5) and an accumulation layer thickness of 2 nm, we deduce superparamagnetic volumes corresponding to disk-shaped clusters of diameter ~4 to 12 nm (Fig. 4D, right axis). Inhomogeneities in the EDL or at the FeS_2 crystal surface could be responsible for this nanoscopic magnetic inhomogeneity, rendering the 16 K scale a superparamagnetic blocking temperature. However, there are at least two issues with this picture. First, as shown in Fig. 4D, the deduced $\mu_c(T)$ has non-negligible T dependence, meaning that the expected H/T scaling of a Langevin function is not exactly obeyed. Second, in this interpretation, the true T_C would be as high as ~280 K, around double the maximum T_C of bulk $Fe_{1-x}Co_xS_2$, which is also only reached at high x. We thus view it as unclear whether the high T behavior in Fig. 3D is best viewed as a paramagnet with strong ferromagnetic correlations persisting to high T or as a superparamagnet. Vitally, however, regardless of interpretation of Figs. 3 and 4 in terms of a ferromagnetic to paramagnetic transition or a ferromagnetic (blocked) to superparamagnetic (unblocked) transition, voltage-induced ferromagnetism in diamagnetic FeS_2 remains clear.

In terms of rationalization of the V_g-induced ferromagnetism in FeS_2 EDLTs, we first note that quantitative comparison to $Fe_{1-x}Co_xS_2$ supports feasibility of induction of a ferromagnetic state. Prior work on $Fe_{1-x}Co_xS_2$ crystals found ferromagnetism to emerge with $T_C \approx 1$ to 2 K at a doped electron density of ~1×10^{20} cm^{-3} (*35*). This is equivalent to a 2D surface density of ~2×10^{13} cm^{-2}, assuming a four unit cell accumulation layer (see fig. S3). These 2D densities are easily achievable in EDLTs (*8*–*10*), although quantitative comparison is frustrated by the fact that the anomalous Hall effect overwhelms the ordinary Hall effect at high V_g (consider Fig. 3, A, B, and D where there is no indication of a negative high H slope at low T), precluding quantification of induced electron densities.

Further insight is provided by first-principles electronic structure calculations, which have been previously applied to $Fe_{1-x}Co_xS_2$ (*52*). Hubbard U–corrected density functional theory (DFT + U) using approaches described in Materials and Methods (*53*, *54*) was used to first reproduce the known crystal and electronic structures of FeS_2. Electrostatic gating was then simulated by artificially adding electrons to the FeS_2 unit cell to the 3D and projected 2D densities shown in Fig. 5 (top and bottom axes, respectively). The magnetization (M) was then extracted versus electron density, resulting in the colored points in the main panel. Ferromagnetic magnetization is found to emerge above ~3×10^{14} cm^{-2}, which, critically, is again

within realistic capabilities of IL gating (*8*–*10*). Note that the magnetization eventually reaches 1 μ_B per Fe, consistent with the half-metallicity, or at least high spin polarization, in $Co_{1-x}Fe_xS_2$ (*37*–*39*, *52*). Additional understanding of the origin of the induced ferromagnetism was obtained from Wannier function–based (*55*) tight-binding parameterization of the DFT-calculated FeS_2 conduction band structure, followed by calculation of the filling-dependent susceptibility $\chi(\underline{k})$ (see Materials and Methods). The resulting $\chi(\underline{k})$ is shown in the inset in Fig. 5, color-coded to the electron densities in the main panel. As the density is increased, a single peak in $\chi(\underline{k})$ emerges at the Γ point ($\underline{k}$ = 0), demonstrating instability toward long-range ferromagnetism, apparently of Stoner type. The threshold filling for the onset of ferromagnetism corresponds to the point at which the Fermi level moves from sulfur *p* states in the lower region of the conduction band to Fe e_g states. These calculations thus confirm the feasibility of ferromagnetism in FeS_2 induced solely by filling of a narrow e_g band, strongly supporting the experimental findings. More detailed calculations will be reported elsewhere, clarifying the different mechanisms and doping thresholds for ferromagnetism in Co-doped and electrostatically doped FeS_2 (*56*).

Additional insight into the V_g-induced insulator-metal and diamagnet-ferromagnet transition is provided by V_g sweep data (Fig. 6). The resistance (R) during a 5 mV s^{-1} ± 4 V cycle at 240 K is shown in Fig. 6A; this temperature was chosen to be as low as possible (to maximize the R modulation) while maintaining tolerable ion mobility in the IL (see Materials and Methods). Unlike the data in Figs. 1 to 4, which were acquired after a 30 min saturating V_g application (see Materials and Methods), these data reveal gating dynamics. Substantial hysteresis is apparent in Fig. 6A, with a consequent sweep rate dependence (fig. S4). Given the evidence of predominantly electrostatic gating, this hysteresis is ascribed not to electrochemistry at the FeS_2 surface but rather to limited ion mobility in the IL, as expected in a macroscopic side-gate device at this T (*10*, *57*). Beginning at V_g = 0, R is seen to rapidly increase with increasing V_g, reaching a peak at 1.5 V, at about twice the initial R. Further increasing V_g then induces a precipitous drop to ~1.5 kilohm, which is maintained as V_g is decreased back to 0 V. R is thus bistable at V_g = 0 due to hysteresis associated with IL dynamics. Negative V_g then increases R to a small, broad peak at −2 V and ~24 kilohm, R remaining relatively constant out to −4 V and back to −1 V. Simply, we interpret the peak at small positive V_g as a characteristic signature of the previously deduced surface inversion. Specifically, R first increases with positive V_g due to depletion of the initially p-type surface, reaching a peak at the compensation point, limited only by bulk conduction. Further increasing V_g then accumulates electrons, rapidly decreasing R. Under the slow gating in Fig. 1B (see Materials and Methods), this inversion is already complete in the +1 V $R_s(T)$, highlighting the complementary information in Fig. 6A. As shown in fig. S5, resistance anisotropy also peaks at the +1 V compensation point in Fig. 6A, likely due to gating inhomogeneity at the highly sensitive compensation point; these factors will also play a role in the more subtle inversion from n- to p-type on reversing V_g in Fig. 6A.

Further supporting the above, Hall data at the indicated V_g are shown in Fig. 6 (C to J) (color coded to the points in Fig. 6A), taken by pausing loops such as Fig. 6A and then rapidly cooling to 180 K. This cooling freezes the IL, thus achieving sufficiently stable resistances

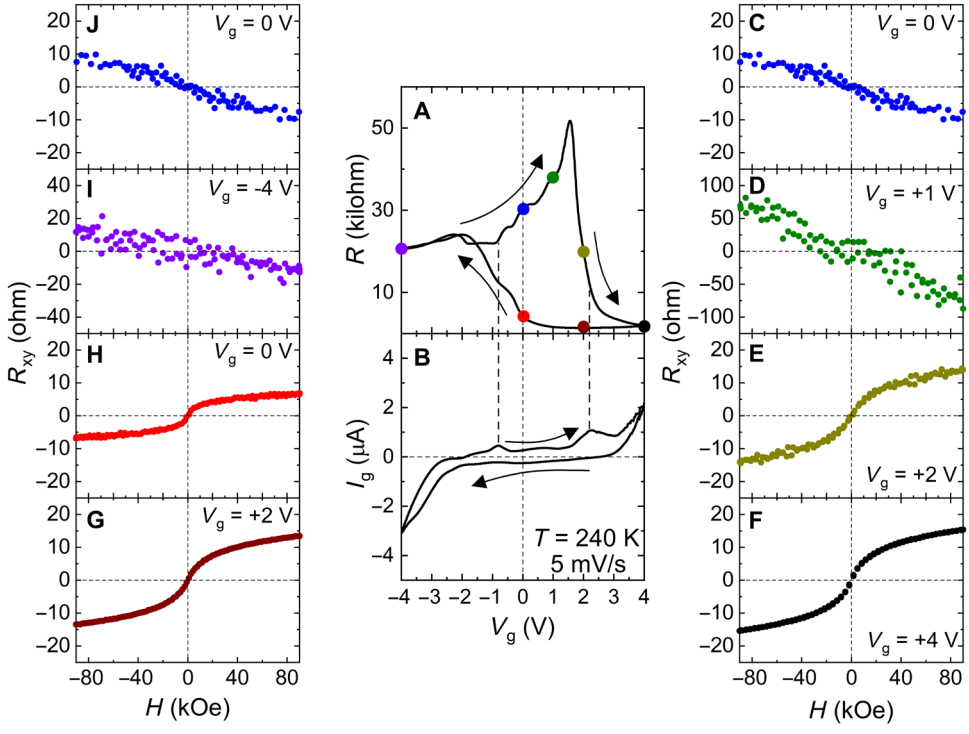

Fig. 6. Hysteretic gate voltage response at 240 K. Gate voltage (V_g) dependence of (**A**) the sample resistance (R) (in one van der Pauw orientation) and (**B**) the gate current (I_g) during a sweep (5 mV/s) at 240 K for sample 2. At this temperature, the IL is in the liquid state, with workable ion mobility. Panels (**C**) to (**J**) show transverse (Hall) resistance (R_{xy}) versus applied magnetic field (H) plots at the gate voltages indicated by the colored solid points in (A); the Hall data are color-coded to these points. Note that the Hall data were acquired after cooling to 180 K, not at 240 K, to minimize measurement drift by freezing the IL. The vertical dashed lines in (A) and (B) highlight the simultaneity of the large changes in R with the I_g peaks. DEME/TFSI was used in all data in this figure.

to permit Hall measurements. At V_g = 0 (Fig. 6C), $R_{xy}(H)$ is near linear with a negative slope due to the small (hopping-suppressed) surface contribution but finite n-type bulk contribution. The situation is similar at +1 V (Fig. 6D), although the increased surface resistance (Fig. 6A) now drives additional bulk current, increasing the magnitude of the Hall slope. However, marked changes occur at +2 V (Fig. 6E), where $R_{xy}(H)$ transforms to a nonlinear sigmoidal shape with positive slope. As already discussed, this occurs due to a positive anomalous Hall coefficient, the anomalous Hall effect arising from ferromagnetic correlations that extend far above T_C at high positive V_g. Figure 6E is thus consistent with Fig. 6A, where R is falling precipitously at +2 V, indicating transformation to the n-type ferromagnetic metallic state. Also consistent with Fig. 6A, the positive slope sigmoidal $R_{xy}(H)$ is maintained at +4, +2, and 0 V (Fig. 6, F to H) due to persistence of the magnetic state. This is then lost on going from 0 to −4 V (compare Fig. 6, H and I), panels (I) and (J) in Fig. 6 being similar to panels (C) and (D) in Fig. 6. Last, we note that the corresponding gate current (I_g) sweep in Fig. 6B is also consistent with the above. The overall form is typical of electrostatically functioning EDLTs, ascending and descending V_g sweeps inducing positive and negative I_g, respectively, due to charging and discharging. These currents are small for such a macroscopic device (<0.5 μA), except at $|V_g| > 3$ V, which we attribute to the electrochemical stability window of the IL. The only additional features are small peaks on the ascending V_g sweep at −1 and 2 V, which (see the vertical dashed lines) correspond to the onset and completion of surface inversion.

CONCLUSIONS

Detailed experimental evidence has been presented establishing that semiconducting diamagnetic FeS_2 with a zero-spin electronic configuration can be electrolyte-gated into a ferromagnetic metallic state in single-crystal EDLTs. A predominantly electrostatic gating mechanism is concluded, driving inversion of the initially p-type FeS_2 surface to an n-type ferromagnetic metal with voltage-tunable T_C up to 25 K. Computational and analytical theory support this, demonstrating feasibility of inducing ferromagnetism by band filling alone. State-of-the-art electrolyte gating is thus capable of inducing surface ferromagnetism in even nonmagnetic materials, with deep implications. Future work could focus on theoretical identification and experimental verification of other diamagnets in which ferromagnetism can be induced, extension to thin films, further exploration of the nature of the voltage-induced ferromagnetism (including the ferromagnetic anisotropy and the issue of paramagnetism versus superparamagnetism), enhancement of the induced T_C, and demonstration of important device function. The latter could include generation of voltage-controlled highly spin-polarized surface currents for spin injection into diamagnetic interiors or overlying heterostructures, representing a small fraction of the possibilities opened up by this work.

MATERIALS AND METHODS

Crystal and device preparation

Pyrite FeS_2 single crystals were grown using chemical vapor transport, as described earlier (*42*, *43*, *47*). Precursor FeS_2 powder was first synthesized by reacting Fe (99.998% purity; Alfa Aesar) and S (99.9995% purity; Alfa Aesar) powders in evacuated quartz ampoules at 500°C for 6 days, followed by repeated grinding and reaction until phase-pure pyrite FeS_2 was obtained by powder x-ray diffraction. Quartz ampoules were then loaded with 2.2 g of this precursor FeS_2, 100 mg of $FeBr_2$ transport agent (99.999% purity; Sigma-Aldrich), and additional S powder (0.06 g for sample 1 and 0.34 g for samples 2 and 3), followed by evacuation to ~10^{-6} torr and flame sealing. The ampoule was then placed in a two-zone furnace for a 17-day growth with the source and growth zones at 670° and 590°C, respectively [after a 3-day inversion period (*42*, *43*, *47*)]. Detailed characterization was presented earlier (*42*, *43*, *47*), indicating phase purity, total metals-basis impurity concentrations of <40 parts per million, and unit cell–level surface roughness. Select structural and chemical characterization data are provided in fig. S1 and table S1. As described in prior work (*43*), lower S loading (as for sample 1) leads to increased S vacancy density and n-type doping and thus lower bulk resistivity.

Crystals were prepared for transport by polishing from the opposite side of a large facet (with SiC grinding paper and diamond slurries down to 3 μm) to thicknesses of ~200 μm, followed by sequential ultrasonication in acetone, methanol, and isopropanol. Au contacts (~50 nm thick) were then sputtered on the pristine (i.e., unpolished) facet. Crystals were then placed on an Al_2O_3 wafer with an Au-coated quartz cylinder, which served as both a high-area gate electrode and liquid container. Two ILs were used: 1-ethyl-3-methylimidazolium bis(trifluoro-methylsulfonyl) imide (EMI/TFSI) and diethylmethyl(2-methoxyethyl)ammonium TFSI (DEME/TFSI).

Electronic transport measurements

Four-terminal van der Pauw resistance measurements [as well as gate voltage (V_g) application and gate current measurement] were achieved with Keithley 2400 source-measure units in a commercial cryostat from 1.4 to 300 K in perpendicular magnetic fields to 9 T. In Figs. 1 to 4, V_g was applied at 300 K for ~30 min, followed by cooling to the base temperature or the temperature shown before warming or sweeping field. EMI/TFSI was the IL for these measurements. In contrast, the V_g sweep in Fig. 6 (A and B) was collected by cooling to 240 K at V_g = 0, followed by sweeping V_g from 0 to 4 V to −4 to 0 V at 5 mV s^{-1} using DEME/TFSI as the IL. This IL was selected in this case as its lower melting point than EMI/TFSI-enabled V_g sweeps at lower temperature, where surface conduction is more dominant, and the dynamic range in sample resistance is thus higher. The 0 to 4 V to −4 to 0 V voltage sequence was repeated until no qualitative features of the hysteresis loop changed in subsequent loops (the loop in Fig. 6 was the third taken). A subsequent and final V_g loop was then performed to collect the Hall data in Fig. 6 (C to J). At each V_g shown in Fig. 6 (C to J), the 240 K V_g sweep was paused, the sample was cooled to 180 K at ~10 K min^{-1}, Hall data were collected, the sample was returned to 240 K, and the V_g sweep was continued. The cooling to 180 K (below the melting point of DEME/TFSI) was done to minimize drift during the Hall sweep.

Theoretical methods

First principles calculations were performed with DFT with a Hubbard U correction (i.e., DFT + U) using the Vienna ab-initio simulation package implementation of the projector-augmented-wave (PAW) approach (*53*, *54*). The PBEsol-generalized gradient approximation was used to approximate the exchange-correlation functional. A Γ-centered 8 × 8 × 8 k-point grid and a plane wave cutoff of 500 eV were used. As discussed elsewhere (*56*), U = 5 eV was used for these calculations, achieving agreement with FeS_2 lattice constants and S—S bond lengths to within <1 and <2.5%, respectively. Electrostatic

gating was then simulated by varying the total number of electrons per unit cell, with the highest level considered being 0.5 added electrons per Fe ion (see Fig. 5). The ion positions and lattice vectors were allowed to relax at each electron concentration. The magnetization per Fe ion was then calculated by integrating the magnetization density over the whole cell and dividing by the number of Fe ions. Following this, a Wannier function–based (*55*), tight-binding model was built using nonspin-polarized DFT calculations as an input, and the electronic susceptibility was then calculated using the Lindhard function. More detailed theoretical results will be reported elsewhere (*56*).

SUPPLEMENTARY MATERIALS

Supplementary material for this article is available at http://advances.sciencemag.org/cgi/content/full/6/31/eabb7721/DC1

REFERENCES AND NOTES

1. F. Hellman, A. Hoffmann, Y. Tserkovnyak, G. S. D. Beach, E. E. Fullerton, C. Leighton, A. H. MacDonald, D. C. Ralph, D. A. Arena, H. A. Dürr, P. Fischer, J. Grollier, J. P. Heremans, T. Jungwirth, A. V. Kimel, B. Koopmans, I. N. Krivorotov, S. J. May, A. K. Petford-Long, J. M. Rondinelli, N. Samarth, I. K. Schuller, A. N. Slavin, M. D. Stiles, O. Tchernyshyov, A. Thiaville, B. L. Zink, Interface-induced phenomena in magnetism. *Rev. Mod. Phys.* **89**, 025006 (2017).
2. D. C. Ralph, M. D. Stiles, Spin transfer torques. *J. Magn. Magn. Mater.* **320**, 1190–1216 (2008).
3. L. Liu, C.-F. Pai, Y. Li, H. W. Tseng, D. C. Ralph, R. A. Buhrman, Spin-torque switching with the giant spin hall effect of tantalum. *Science* **336**, 555–558 (2012).
4. I. M. Miron, K. Garello, G. Gaudin, P.-J. Zermatten, M. V. Costache, S. Auffret, S. Bandiera, B. Rodmacq, A. Schuhl, P. Gambardella, Perpendicular switching of a single ferromagnetic layer induced by in-plane current injection. *Nature* **476**, 189–193 (2011).
5. S. Manipatruni, D. E. Nikonov, I. A. Young, Beyond CMOS computing with spin and polarization. *Nat. Phys.* **14**, 338–343 (2018).
6. A. Molinari, H. Hahn, R. Kruk, Voltage-control of magnetism in all-solid-state and solid/liquid magnetoelectric composites. *Adv. Mater.* **31**, e1806662 (2019).
7. C. Navarro-Senent, A. Quintana, E. Menéndez, E. Pellicer, J. Sort, Electrolyte-gated magnetoelectric actuation: Phenomenology, materials, mechanisms, and prospective applications. *APL Mater.* **7**, 030701 (2019).
8. C. Leighton, Electrolyte-based ionic control of functional oxides. *Nat. Mater.* **18**, 13–18 (2019).
9. S. Z. Bisri, S. Shimizu, M. Nakano, Y. Iwasa, Endeavor of iontronics: From fundamentals to applications of ion-controlled electronics. *Adv. Mater.* **29**, 1607054 (2017).
10. S. H. Kim, K. Hong, W. Xie, K. H. Lee, S. Zhang, T. P. Lodge, C. D. Frisbie, Electrolyte-gated transistors for organic and printed electronics. *Adv. Mater.* **25**, 1822–1846 (2013).
11. A. S. Dhoot, C. Israel, X. Moya, N. D. Mathur, R. H. Friend, Large electric field effect in electrolyte-gated manganites. *Phys. Rev. Lett.* **102**, 136402 (2009).
12. K. Shimamura, D. Chiba, S. Ono, S. Fukami, N. Ishiwata, M. Kawaguchi, K. Kobayashi, T. Ono, Electrical control of Curie temperature in cobalt using an ionic liquid film. *Appl. Phys. Lett.* **100**, 122402 (2012).
13. Q. Lu, B. Yildiz, Voltage-controlled topotactic phase transition in thin-film $SrCoO_x$ monitored by in situ x-ray diffraction. *Nano Lett.* **16**, 1186–1193 (2016).
14. N. Lu, P. Zhang, Q. Zhang, R. Qiao, Q. He, H.-B. Li, Y. Wang, J. Guo, D. Zhang, Z. Duan, Z. Li, M. Wang, S. Yang, M. Yan, E. Arenholz, S. Zhou, W. Yang, L. Gu, C.-W. Nan, J. Wu, Y. Tokura, P. Yu, Electric-field control of tri-state phase transformation with a selective dual-ion switch. *Nature* **546**, 124–128 (2017).
15. J. Walter, G. Yu, B. Yu, A. Grutter, B. Kirby, J. Borchers, Z. Zhang, H. Zhou, T. Birol, M. Greven, C. Leighton, Ion-gel-gating-induced oxygen vacancy formation in epitaxial $La_{0.5}Sr_{0.5}CoO_{3-\delta}$ films from in *operando* x-ray and neutron scattering. *Phys. Rev. Mater.* **1**, 071403(R) (2017).
16. J. Walter, T. Charlton, H. Ambaye, M. R. Fitzsimmons, P. P. Orth, R. M. Fernandes, C. Leighton, Giant electrostatic modification of magnetism via electrolyte-gate-induced cluster percolation in $La_{1-x}Sr_xCoO_{3-\delta}$. *Phys. Rev. Mater.* **2**, 111406(R) (2018).
17. L. M. Zheng, X. R. Wang, W. M. Lü, C. J. Li, T. R. Paudel, Z. Q. Liu, Z. Huang, S. W. Zeng, K. Han, Z. H. Chen, X. P. Qiu, M. S. Li, S. Yang, B. Yang, M. F. Chisholm, L. W. Martin, S. J. Pennycook, E. Y. Tsymbal, J. M. D. Coey, W. W. Cao, Ambipolar ferromagnetism by electrostatic doping of a manganite. *Nat. Commun.* **9**, 1897 (2018).
18. J. Jeong, N. Aetukuri, T. Graf, T. D. Schladt, M. G. Samant, S. S. P. Parkin, Suppression of metal-insulator transition in VO_2 by electric field–induced oxygen vacancy formation. *Science* **339**, 1402–1405 (2013).
19. M. Li, W. Han, X. Jiang, J. Jeong, M. G. Samant, S. S. P. Parkin, Suppression of ionic liquid gate-induced metallization of $SrTiO_3$(001) by oxygen. *Nano Lett.* **13**, 4675–4678 (2013).
20. H. T. Yi, B. Gao, W. Xie, S.-W. Cheong, V. Podzorov, Tuning the metal-insulator crossover and magnetism in $SrRuO_3$ by ionic gating. *Sci. Rep.* **4**, 6604 (2014).
21. H. Ji, J. Wei, D. Natelson, Modulation of the electrical properties of VO_2 nanobeams using an ionic liquid as a gating medium. *Nano Lett.* **12**, 2988–2992 (2012).
22. X. Leng, J. Pereiro, J. Strle, G. Dubuis, A. T. Bollinger, A. Gozar, J. Wu, N. Litombe, C. Panagopoulos, D. Pavuna, I. Božović, Insulator to metal transition in WO_3 induced by electrolyte gating. *npj Quantum Mater.* **2**, 35 (2017).
23. M. Weisheit, S. Fähler, A. Marty, Y. Souche, C. Poinsignon, D. Givord, Electric field-induced modification of magnetism in thin-film ferromagnets. *Science* **315**, 349–351 (2007).
24. C. Bi, Y. Liu, T. Newhouse-Illige, M. Xu, M. Rosales, J. W. Freeland, O. Mryasov, S. Zhang, S. G. E. te Velthuis, W. G. Wang, Reversible control of Co magnetism by voltage-induced oxidation. *Phys. Rev. Lett.* **113**, 267202 (2014).
25. U. Bauer, L. Yao, A. J. Tan, P. Agrawal, S. Emori, H. L. Tuller, S. van Dijken, G. S. D. Beach, Magneto-ionic control of interfacial magnetism. *Nat. Mater.* **14**, 174–181 (2015).
26. D. A. Gilbert, A. J. Grutter, E. Arenholz, K. Liu, B. J. Kirby, J. A. Borchers, B. B. Maranville, Structural and magnetic depth profiles of magneto-ionic heterostructures beyond the interface limit. *Nat. Commun.* **7**, 12264 (2016).
27. A. J. Tan, M. Huang, C. O. Avci, F. Büttner, M. Mann, W. Hu, C. Mazzoli, S. Wilkins, H. L. Tuller, G. S. D. Beach, Magneto-ionic control of magnetism using a solid-state proton pump. *Nat. Mater.* **18**, 35–41 (2019).
28. J. Zehner, R. Huhnstock, S. Oswald, U. Wolff, I. Soldatov, A. Ehresmann, K. Nielsch, D. Holzinger, K. Leistner, Nonvolatile electric control of exchange bias by a redox transformation of the ferromagnetic layer. *Adv. Electron. Mater.* **5**, 1900296 (2019).
29. L. Herrera Diez, Y. T. Liu, D. A. Gilbert, M. Belmeguenai, J. Vogel, S. Pizzini, E. Martinez, A. Lamperti, J. B. Mohammedi, A. Laborieux, Y. Roussigné, A. J. Grutter, E. Arenholtz, P. Quarterman, B. Maranville, S. Ono, M. S. El Hadri, R. Tolley, E. E. Fullerton, L. Sanchez-Tejerina, A. Stashkevich, S. M. Chérif, A. D. Kent, D. Querlioz, J. Langer, B. Ocker, D. Ravelosona, Nonvolatile ionic modification of the Dzyaloshinskii-Moriya interaction. *Phys. Rev. Appl.* **12**, 034005 (2019).
30. K.-Y. Lee, S. Jo, A. J. Tan, M. Huang, D. Choi, J. H. Park, H.-I. Ji, J.-W. Son, J. Chang, G. S. D. Beach, S. Woo, Fast magneto-ionic switching of interface anisotropy using yttria-stabilized zirconia gate oxide. *Nano Lett.* **20**, 3435–3441 (2020).
31. A. Quintana, E. Menéndez, M. O. Liedke, M. Butterling, A. Wagner, V. Sireus, P. Torruella, S. Estradé, F. Peiró, J. Dendooven, C. Detavernier, P. D. Murray, D. A. Gilbert, K. Liu, E. Pellicer, J. Nogues, J. Sort, Voltage-controlled on–off ferromagnetism at room temperature in a single metal oxide film. *ACS Nano* **12**, 10291–10300 (2018).
32. D. J. Vaughan, J. R. Craig, *Mineral Chemistry of Metal Sulfides* (Cambridge Univ. Press, Cambridge/New York, 1978).
33. X. Zhang, M. Manno, A. Baruth, M. Johnson, E. S. Aydil, C. Leighton, Crossover from nanoscopic intergranular hopping to conventional charge transport in pyrite thin films. *ACS Nano* **7**, 2781–2789 (2013).
34. X. Zhang, T. Scott, T. Socha, D. Nielsen, M. Manno, M. Johnson, Y. Yan, Y. Losovyj, P. Dowben, E. S. Aydil, C. Leighton, Phase stability and stoichiometry in thin film iron pyrite: Impact on electronic transport properties. *ACS Appl. Mater. Interfaces* **7**, 14130–14139 (2015).
35. S. Guo, D. P. Young, R. T. Macaluso, D. A. Browne, N. L. Henderson, J. Y. Chan, L. L. Henry, J. F. DiTusa, Discovery of the Griffiths phase in the itinerant magnetic semiconductor $Fe_{1-x}Co_xS_2$. *Phys. Rev. Lett.* **100**, 017209 (2008).
36. S. Guo, D. P. Young, R. T. Macaluso, D. A. Browne, N. L. Henderson, J. Y. Chan, L. L. Henry, J. F. DiTusa, Charge transport in cobalt-doped iron pyrite. *Phys. Rev. B* **81**, 144424 (2010).
37. L. Wang, K. Umemoto, R. M. Wentzcovitch, T. Y. Chen, C. L. Chien, J. G. Checkelsky, J. C. Eckert, E. D. Dahlberg, C. Leighton, $Co_{1-x}Fe_xS_2$: A tunable source of highly spin-polarized electrons. *Phys. Rev. Lett.* **94**, 056602 (2005).
38. L. Wang, T. Y. Chen, C. L. Chien, J. G. Checkelsky, J. C. Eckert, E. D. Dahlberg, K. Umemoto, R. M. Wentzcovitch, C. Leighton, Composition controlled spin polarization in $Co_{1-x}Fe_xS_2$: Electronic, magnetic, and thermodynamic properties. *Phys. Rev. B* **73**, 144402 (2006).
39. C. Leighton, M. Manno, A. Cady, J. W. Freeland, L. Wang, K. Umemoto, R. M. Wentzcovitch, T. Y. Chen, C. L. Chien, P. L. Kuhns, M. J. R. Hoch, A. P. Reyes, W. G. Moulton, E. D. Dahlberg, J. Checkelsky, J. Eckert, Composition controlled spin polarization in $Co_{1-x}Fe_xS_2$ alloys. *J. Phys. Condens. Matter* **19**, 315219 (2007).
40. J. D. Burton, E. Y. Tsymbal, Highly spin-polarized conducting state at the interface between nonmagnetic bandinsulators: $LaAlO_3/FeS_2$(001). *Phys. Rev. Lett.* **107**, 166601 (2011).
41. M. Limpinsel, N. Farhi, N. Berry, J. Lindemuth, C. L. Perkins, Q. Lin, M. Law, An inversion layer at the surface of n-type iron pyrite. *Energ. Environ. Sci.* **7**, 1974–1989 (2014).
42. J. Walter, X. Zhang, B. Voigt, R. Hool, M. Manno, F. Mork, E. S. Aydil, C. Leighton, Surface conduction in n-type pyrite FeS_2 single crystals. *Phys. Rev. Mater.* **1**, 065403 (2017).
43. B. Voigt, W. Moore, M. Manno, J. Walter, J. D. Jeremiason, E. S. Aydil, C. Leighton, Transport evidence for sulfur vacancies as the origin of unintentional n-type doping in pyrite FeS_2. *ACS Appl. Mater. Interfaces* **11**, 15552–15563 (2019).
44. D. Liang, M. Caban-Acevedo, N. S. Kaiser, S. Jin, *Nano Lett.* **14**, 6754–6760 (2014).
45. B. I. Shklovskii, A. L. Efros, *Electronic Properties of Doped Semiconductors* (Springer, Heidelberg, 1984).

46. P. A. Lee, T. V. Ramakrishnan, Disordered electronic systems. *Rev. Mod. Phys.* **57**, 287–337 (1985).
47. X. Zhang, M. Li, J. Walter, L. O'Brien, M. A. Manno, B. Voigt, F. Mork, S. V. Baryshev, J. Kakalios, E. S. Aydil, C. Leighton, Potential resolution to the doping puzzle in iron pyrite: Carrier type determination by Hall effect and thermopower. *Phys. Rev. Mater.* **1**, 015402 (2017).
48. K. Adachi, K. Sato, M. Okimori, G. Yamauchi, H. Yasuoka, Y. Nakamura, Magnetic anisotropy of CoS_2 –torque and NMR measurements. *J. Physical Soc. Japan* **38**, 81–86 (1975).
49. R. C. O'Handley, *Modern Magnetic Materials : Principles and Applications* (John Wiley and Sons, Inc, New York, 2000).
50. M. Iizumi, J. W. Lynn, A. Ohsawa, H. Ito, Spin-wave and critical scattering of neutrons from cobalt disulfide. *AIP Conf. Proc.* **29**, 266–267 (1976).
51. N. D. Mermin, H. Wagner, Absence of ferromagnetism or antiferromagnetism in one- or two-dimensional isotropic Heisenberg models. *Phys. Rev. Lett.* **17**, 1133–1136 (1966).
52. I. I. Mazin, Robust half metalicity in $Fe_xCo_{1-x}S_2$. *Appl. Phys. Lett.* **77**, 3000 (2000).
53. G. Kresse, J. Furthmüller, Efficient iterative schemes for ab initio total-energy calculations using a plane-wave basis set. *Phys. Rev. B* **54**, 11169–11186 (1996).
54. G. Kresse, D. Joubert, From ultrasoft pseudopotentials to the projector augmented-wave method. *Phys. Rev. B* **59**, 1758–1775 (1999).
55. N. Marzari, A. A. Mostofi, J. R. Yates, I. Souza, D. Vanderbilt, Maximally localized Wannier functions: Theory and applications. *Rev. Mod. Phys.* **84**, 1419–1475 (2012).
56. E. Day-Roberts, T. Birol, R. M. Fernandes, Contrasting ferromagnetism in pyrite FeS_2 induced by chemical doping versus electrostatic gating. *Phys. Rev. Mater.* **4**, 054405 (2020).
57. J. Walter, H. Wang, B. Luo, C. D. Frisbie, C. Leighton, Electrostatic *versus* electrochemical doping and control of ferromagnetism in ion-gel-gated ultrathin $La_{0.5}Sr_{0.5}CoO_{3-\delta}$. *ACS Nano* **10**, 7799–7810 (2016).

Acknowledgments: We gratefully acknowledge E. S. Aydil for his role in shaping our understanding of electronic transport in FeS_2 crystals, forming a foundation for this work. **Funding:** This work was primarily supported by the NSF through the University of Minnesota (UMN) MRSEC under DMR-1420013. Parts of the work were carried out in the Characterization Facility, UMN, which receives partial support from NSF through the MRSEC program. Portions of this work were also conducted in the Minnesota Nano Center, which is supported by the NSF through the National Nano Coordinated Infrastructure Network under NNCI-1542202. The Minnesota Supercomputing Institute is acknowledged for providing resources that contributed to the research results reported. **Author contributions:** C.L. and J.W. conceived the study. J.W. and B.V. performed the measurements, assisted by K.H., on single crystals grown and characterized by B.V. and J.W. Supervision of all aspects of the experimental work was provided by C.L. Calculations were performed by E.D.-R. and supervised by T.B. and R.M.F. The paper was written by J.W. and C.L. with input from all authors. **Competing interests:** The authors declare that they have no competing interests. **Data and materials availability:** All data needed to evaluate the conclusions in the paper are present in the paper and/or the Supplementary Materials. Additional data related to this paper may be requested from the authors.

Submitted 22 March 2020
Accepted 12 June 2020
Published 29 July 2020
10.1126/sciadv.abb7721

Citation: J. Walter, B. Voigt, E. Day-Roberts, K. Heltemes, R. M. Fernandes, T. Birol, C. Leighton, Voltage-induced ferromagnetism in a diamagnet. *Sci. Adv.* **6**, eabb7721 (2020).

ScienceAdvances

Voltage-induced ferromagnetism in a diamagnet

Jeff WalterBryan VoigtEzra Day-RobertsKei HeltemesRafael M. FernandesTuran BirolChris Leighton

Sci. Adv., 6 (31), eabb7721. • DOI: 10.1126/sciadv.abb7721